
This is an electronic reprint of the original article.
This reprint may differ from the original in pagination and typographic detail.

Ullah, Rizwan; Lian, Junhe; Akmal, Jan Sher; Wu, Jiaojiao; Niemi, Esko

Prediction and validation of melt pool dimensions and geometric distortions of additively manufactured AlSi10Mg

Published in:
International Journal of Advanced Manufacturing Technology

DOI:
[10.1007/s00170-023-11264-w](https://doi.org/10.1007/s00170-023-11264-w)

Published: 01/06/2023

Document Version
Publisher's PDF, also known as Version of record

Published under the following license:
CC BY

Please cite the original version:
Ullah, R., Lian, J., Akmal, J. S., Wu, J., & Niemi, E. (2023). Prediction and validation of melt pool dimensions and geometric distortions of additively manufactured AlSi10Mg. *International Journal of Advanced Manufacturing Technology*, 126(7-8), 3593-3613. <https://doi.org/10.1007/s00170-023-11264-w>

This material is protected by copyright and other intellectual property rights, and duplication or sale of all or part of any of the repository collections is not permitted, except that material may be duplicated by you for your research use or educational purposes in electronic or print form. You must obtain permission for any other use. Electronic or print copies may not be offered, whether for sale or otherwise to anyone who is not an authorised user.



Prediction and validation of melt pool dimensions and geometric distortions of additively manufactured AlSi10Mg

Rizwan Ullah¹ · Junhe Lian¹ · Jan Akmal¹ · Jiaojiao Wu¹ · Esko Niemi¹

Received: 18 October 2022 / Accepted: 12 March 2023 / Published online: 4 April 2023
© The Author(s) 2023

Abstract

A finite element–based thermomechanical modeling approach is developed in this study to provide a prediction of the mesoscale melt pool behavior and part-scale properties for AlSi10Mg alloy. On the mesoscale, the widely adopted Goldak heat source model is used to predict melt pool formed by laser during powder bed fusion process. This requires the determination of certain parameters as they control temperature distribution and, hence, melt pool boundaries. A systematic parametric approach is proposed to determine parameters, i.e., absorption coefficient and transient temperature evolution. The simulation results are compared in terms of morphology of melt pool with the literature results. Considering the part-scale domain, there is increasing demand for predicting geometric distortions and analyzing underlying residual stresses, which are highly influenced by the mesh size and initial temperature setup. This study aims to propose a strategy for evaluating the correlation between the mesh size and the initial temperature to provide correct residual stresses when increasing the scale of the model for efficiency. The outcomes revealed that the predicted melt pool error produced by optimal Goldak function parameters is between 5 and 12%. On the part-scale, the finite element model is less sensitive to mesh size for distortion prediction, and layer-lumping can be used to increase the speed of simulation. The effect of large time increments and layer lumping can be compensated by appropriate initial temperature value for AlSi10Mg. The study aids practitioners and researchers to establish and validate design for additive manufacturing within the scope of desired part quality metrics.

Keywords FE simulation · Powder bed fusion · Thermal history · Layer and time-lumping · Residual stress prediction

1 Introduction

The impact of additive manufacturing (AM) in today's world is undoubtedly all-time high ranging from low-cost and educational applications to high-performance complex engineering components. AM is emerging into a general-purpose technology enabling industry 4.0 and offering a plethora of applications [1–4]. Out of the seven ISO/ASTM registered technologies, powder bed fusion (PBF) process is widely used for manufacturing metal AM components using laser as thermal input and metal powder as raw material [4, 5]. Metal powder (particle diameter ranging from 20 to 80 μm) is spread via a recoater/spreader, and as the second step, laser travels on predefined paths to melt the metal particles, which upon cooling solidify to create the final shape. Terms

such as selective laser sintering (SLS), direct metal laser sintering (DMLS), and sometimes simply laser sintering (LS) refer to identical manufacturing process. As research and development in PBF is rapidly increasing, more engineering materials that can be processed by laser sintering are commercially available, e.g., aluminum alloys, cobalt-chrome, steels, copper, titanium alloys, and nickel alloys.

At the same time, significant efforts are put into improving the quality of AM-manufactured components due to the existence of process-induced defects, whether related to the geometry (shrinkages, warpage), surface defects [6] (pores, dross, etc.), or the anisotropy [7] in material properties. Thermomechanical simulation [8, 9], and inherent strain approach [10, 11] are two types of finite element (FE)–based simulation techniques frequently used for predicting properties of additively manufactured components ranging from melt pool prediction [12–14] to final residual stresses [15] and component distortions. Thermomechanical simulation is a more systematic and sequential approach in which the first step thermal analysis (TA) yields a transient temperature

✉ Rizwan Ullah
rizwan.ullah@aalto.fi

¹ Advanced Manufacturing and Materials, Mechanical Engineering Department, Aalto University, Espoo, Finland

field, which is used as the thermal load to drive the subsequent mechanical analysis (MA) step. On the other hand, the inherent strain approach is relatively fast and requires thermal strain in the MA step to predict final component distortions and residual stresses.

During the PBF process, laser acts as a material activating source and scans usually at very high speeds [16]. Similarly, melt pool formation and solidification is a rapidly evolving process [17]. Capturing such fluctuating transient temperature evolution using thermomechanical simulation is only possible using micrometer-level mesh and microseconds-level time increments to solve partial differential equations. This high-fidelity configuration is appropriate for mesoscale which can vary between 0.01 and 1 mm [18]. Temperature and temperature gradient evolution affect the solidification, phase transformation, and microstructure of the material. In addition to affecting grain boundaries and dislocation types, microstructural features also have a decisive impact on AM-induced residual stresses [19], leading to AM defects [6]. On the other hand, most of the time it is more practical to determine the final distortions of the component after it is manufactured/printed. This part-scale (larger than 1 mm but typically larger than tens of mm) domain requires mesh size and time-increment selection to be large in order for simulation to be completed in hours or days.

During thermal simulation setup, accurate evolving temperature also requires detailed temperature-dependent thermal and mechanical properties of a material. This can be validated either by comparing in situ temperature measurement with the simulation predicted transient temperature or melt pool size with the experimentally measured melt pool after solidification. Among the many parameters which affect the temperature prediction during PBF simulation, laser properties (speed, power, absorptivity), printing strategy (hatch distance [20], laser path rotation [21]), layer thickness, convection coefficient, and heat source model are the crucial ones. The metal powder generally has more tendency to absorb laser power compared to the same solid material due to its porous nature [22].

Various mathematical expressions defining laser heat source models have been reported [23, 24] that differ in terms of the required computational resources and accuracy of the melt pool prediction in a thermomechanical analysis. Goldak heat model [25] is one of the accurate models requiring high computations while others, e.g., the line heat source model and some volumetric heat sources [26], are less precise but computationally efficient. Defining a melt pool via the Goldak model requires the determination of controlling parameters that are determined considering the temperature-dependent thermal properties of the material. While Goldak function parameters are reported frequently for some metal powders, there are limited research studies on Goldak controlling parameters for AlSi10Mg.

To speed up the simulation for predicting part-scale properties (residual stresses and distortions), sometimes

lumping techniques [27–29] are employed where many powder layers are merged into a single big element. Similarly, certain heat source models requiring less computational resources become very effective in this context. These approximations can potentially lead to underestimation or often overestimation of induced distortions [28]. Liang et al. [11] have proposed modifications for the inherent strain approach. Similarly, Yang et al. [8] have defined an additional simulation parameter (initial temperature) to accurately predict residual strains and distortions. It has been observed that such compensation effects are not well studied for distortion prediction of AlSi10Mg.

Although many ready-made FE-based commercial softwares are available that can simulate PBF, directed laser deposition (DLD), or other AM processes, the accuracy of underlying simulation strategies need to be compared with customized general purpose FE packages, e.g., Abaqus, Ansys, etc. From the literature, it has been observed that studies covering the simulation of additively manufactured built part removal via electron discharge machining (EDM) from the substrate are limited, and thus needs to be investigated. Furthermore, according to the authors' best knowledge, there have been very few FE simulation-based studies that combine prediction of the melt pool at the meso-scale and macro properties, such as geometric distortions for additively manufactured AlSi10Mg alloy. This is due to the reason that either the focus is mainly on the temperature evolution and melt pool formation [30–33] or entirely on predicting part-scale properties such as geometrical defects [34, 35]. This research fills this gap by formulating a thermomechanical simulation of the PBF process for AlSi10Mg using Abaqus. Special purpose AM techniques of Abaqus can assist AM simulation and have been very effective in predicting transient temperature evolution [36] and part-scale properties [8].

In this research, the Goldak function parameters are determined for AlSi10Mg using an inverse technique for a meso-scale model with a full factorial design of experiments. Melt pools predicted by optimal Goldak parameters are validated with the literature based melt pool dimensions. The effect of metal powder absorptivity and inter-layer laser delay time on temperature evolution is determined. For the part-scale domain, two mesh sizes, compensation parameters (initial temperature), and built part removal from the substrate have been studied for the prediction of PBF-induced distortions for the thin plates of AlSi10Mg.

2 Governing equations

2.1 Thermal analysis

During thermal analysis in the PBF process, powder particles are melted using laser power and heat input raises the

temperature of metal powder. Heat transfer by conduction mechanism in three-dimensional space is governed as:

$$\rho c_p \frac{dT}{dt} - \nabla \cdot (k \nabla T) = 0 \tag{1}$$

Here ρ , c_p and k represent material density, specific heat and thermal conductivity.

In addition, heat transfer occurring through convection and radiation can be modeled respectively with Eq. (2) and Eq. (3), with h being the convective heat transfer coefficient, σ Stephen Boltzmann constant and ε being the emissivity.

$$Q_{convection} = h(T - T_\infty) \tag{2}$$

$$Q_{radiation} = \varepsilon \sigma (T^4 - T_\infty^4) \tag{3}$$

At the beginning of the analysis, the initial temperature T_o , is specified as representing the ambient temperature of the metal powder system.

$$T(x, y, z, t)|_{t=0} = T_o \tag{4}$$

2.2 Mechanical analysis

In a sequential thermal-stress analysis, temperature field from thermal analysis is applied as a thermal load to the mechanical analysis. Equation (5) governs mechanical equilibrium.

$$\nabla \sigma + F_v = 0 \tag{5}$$

where σ and F_v are representing Cauchy stress tensor and body force.

Stress-strain relationship in a standard form can be expressed as:

$$\sigma = C : \varepsilon \tag{6}$$

where ε is the total strain and further consists of sum of an elastic strain (ε_e), plastic strain (ε_p) and a thermal strain (ε_{th}).

$$\varepsilon = \varepsilon_e + \varepsilon_p + \varepsilon_{th} \tag{7}$$

To model the plastic deformations, flow stress curves representing relationship between the applied stress and the resulting plastic strain are defined. In this research orthotropic hardening for plasticity is adopted [8].

In a FE analysis of the PBF process, rapid melting and solidification process of melt pool result in thermal strain accumulation which affects the total strain, resulting in residual stresses and distortions in the mechanical analysis. Equation (8) enforces the initial condition of zero-strain case for the newly added layer and imposes thermal contractions after layer deposition in a FE analysis.

$$\varepsilon_{th} = \alpha (T - T_o) - \alpha (T_{initial} - T_o) \tag{8}$$

Here, T_o represents the reference temperature for thermal expansion coefficient, T is current Temperature, α denotes thermal expansion coefficient and $T_{initial}$ is the initial temperature for mechanical analysis.

Finally, the total strain associated with a deposited layer ε^i is affecting the displacement (u) of the activated layer as defined by Eq. (9).

$$\varepsilon^i = \frac{1}{2} [\nabla u^i + (\nabla u^i)^T] \tag{9}$$

3 Material and methodology

During the study, meso-scale is considered to be in the range of 0.01–1 mm while part-scale is assumed to be larger than 1 mm.

3.1 Powder bed fusion

Three rectangular plates of aluminum alloy AlSi10Mg (Fig. 1) were printed of varying thickness (1, 2, and 3 mm) using the EOS M290 (EOS GmbH, Krailling, Germany) machine, which follows the PBF process. Out of multiple thin plates for one particular thickness in Fig. 1, only one thin plate from each set was measured for determining geometric dimensions. Table 1 lists the printing parameters. Figure 2 depicts nomenclature of deposited layers in a typical printing configuration. Upskin area constitutes the top few surface layers with no laser rotation. Number of layers (as indicated by Fig. 2) can be more than one to ensure that results of customized printing parameters — no porosity and low surface roughness can be achieved. The infill area represents core material (bulk of material) where laser rotates 67° with each deposited layer. Downskin surfaces are usually at the bottom of the built part and typically contain surfaces in contact with the loose powder beneath. This differentiation as a function of printing parameters is adopted to optimize certain quality features of the built part.

3.2 Finite element simulation

A FE thermomechanical model is built using Abaqus special purpose additive manufacturing techniques [36, 37] to simulate thermal analysis (TA) for a meso-scale model to analyze transient temperature behavior, absorptivity and most importantly to predict and validate the melt pool dimensions using the Goldak function as heat input model. In the second part of this research, PBF-induced geometric distortions are predicted using sequentially coupled TA and mechanical

Fig. 1 Printed aluminum thin plates: schematics, units [mm] (a), actual printed parts (b)

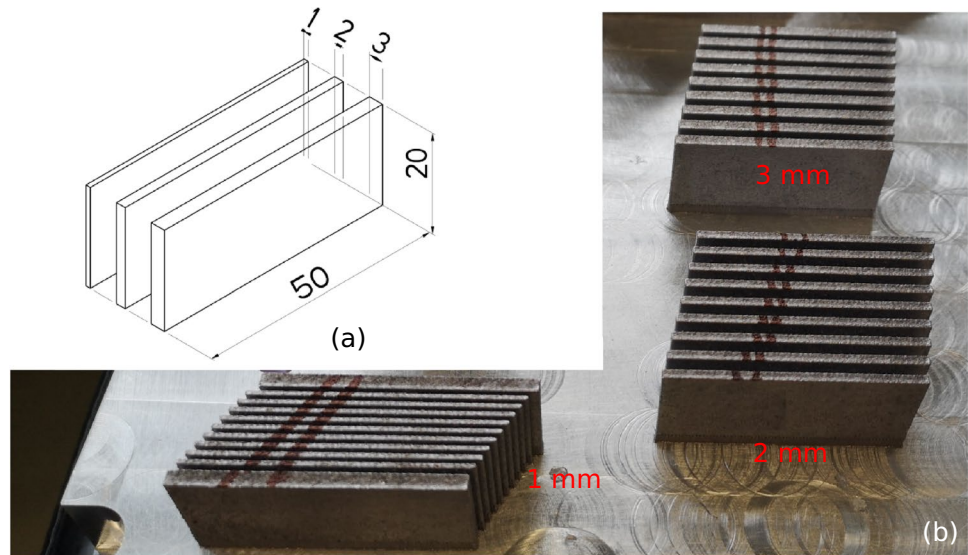


Table 1 Printing parameters used for real time printing

	Contour	Infill	Up-skin
Power	320 W	370 W	360 W
Speed	560 mm/s	1300 mm/s	1000 mm/s
Hatch distance		0.13 mm	0.21 mm
Energy	19.05 J/mm ³	72.98 J/mm ³	57.14 J/mm ³
Layer thickness	0.03 mm		
Cooling time between layers	45 s approx		
Average Laser shut off time (within one layer)	5 milli seconds		
Substrate temperature	35°C		
Ambient temperature	26°C		
Laser beam diameter	0.080 mm		
Rotation of layers	–	67°	No rotation
Roller speed	150 mm/s		
Laser name and specification	Yb-fibre laser 400W (IPG laser GmbH), 1060–100 nm, pulsating 960–980 nm, f-theta lens		
Inert gas	Argon		
Gas pressure	26 milli bar		
Supports used	Supports are created by Materialise Magics 25.0 Standard block support (3 mm) and 4–6 solid cones		
Software used	EOSPRINT 2.6		

analysis (MA) for AISi10Mg material. The temperature dependent thermal and mechanical properties considered during the FE simulation are listed in Tables 2 and 3.

3.2.1 Meso-scale model: melt pool prediction and temperature evolution (high fidelity)

A meso-scale model (Fig. 3) has been employed to predict the melt pool dimensions and to analyze the temperature

evolution for a single-pass and multi-layer cases for AISi10Mg in a TA step. In a FE model, real powder bed of PBF is replaced by 3D continuum elements with mesh size of 15 μm and termed as powder-bed. Real powder layer (RPL) thickness during the PBF was 30 μm which in FE model is replaced by the two elements along z-axis, in a meso-scale model.

The Goldak function as heat source model [25] (Eq. (10) and Fig. 4) is used as heat source model to transfer heat

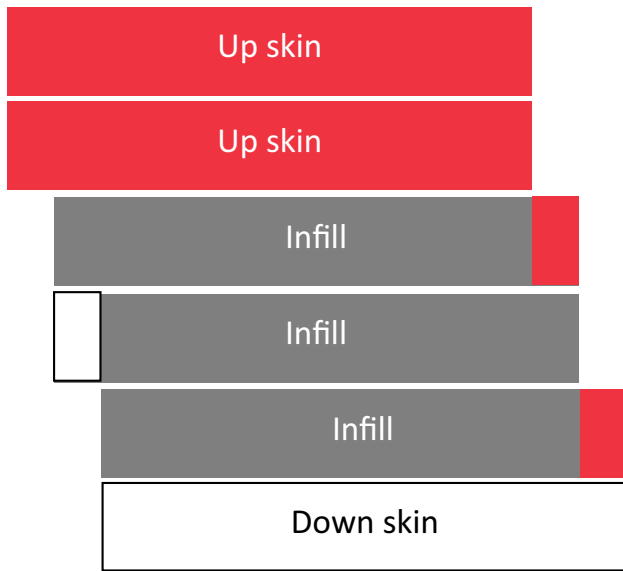


Fig. 2 Deposited layers nomenclature

energy from the laser to the powder-bed. The concerned Goldak function parameters (‘a’, ‘b’, ‘c_f’ and ‘c_r’) affect the temperature distribution in the melt pool considering temperature dependent thermal properties of AlSi10Mg and, hence, control melt pool dimensions. Parameters ‘a’, ‘b’, ‘c_f’ and ‘c_r’ represent half of melt pool width, melt pool depth, front melt pool length and rear melt pool length respectively and control double ellipsoidal shape of the melt pool. Parameter $f_{f/r}$ controls the amount of heat fraction added to the front and the rear melt pool areas and follow $f_f + f_r = 2rule$, [41]. Absorbed power Q_w , highly depends on powder absorptivity for which coefficient of heat absorption η is defined by Eq. (11)

$$Q_{r/f} = \frac{6\sqrt{3}f_{f/r}Q_w}{abc_{f/r}\pi} e^{(-\frac{3x^2}{r^2})} e^{(-\frac{3y^2}{a^2})} e^{(-\frac{3z^2}{b^2})} \tag{10}$$

$$Q_w = \eta P \tag{11}$$

Here, P represents total input laser power. To simplify the search of optimal Goldak function parameters, there could be five unknown parameters (η , ‘a’, ‘b’, ‘c_f’ and ‘c_r’) related to the melt pool dimensions. M. Tang [42] has measured the melt pool dimensions for the up-skin layer (laser parameters: 360 W and 1000 mm/s) and reported width and depth of the melt pool are listed in Table 4.

Ming’s [42] average melt pool dimensions have been taken as a reference case in this research and are predicted using FE meso-scale model to figure out unknown Goldak function parameters as well as optimal absorption coefficient value.

In the meso-scale model, the substrate is meshed using coarser elements (0.1 mm and 0.5 mm). Initial pre-defined temperature for the powder-bed and substrate is set to 26 °C and 35 °C (as per Table 1) to match with the real print settings. A transient heat transfer analysis is performed using a time increment of 20 μ s.

Up-skin region As a first step, modified Rosenthal equation [42] has been used to determine the absorption coefficient η (Eq. (11)) for the top layer in up-skin region using reported melt pool depth by Ming [42]. Here k , C , ρ , T , T_0 , V , D represent thermal conductivity, specific heat, density, solidus temperature, pre-heating temperature, laser speed and depth of melt pool respectively. Rosenthal equation has been solved using room temperature thermal properties.

Table 2 AlSi10Mg, temperature dependent thermal and mechanical properties [38–40]

Temp [°C]	Thermal conductivity [mW/(mm·°C)]	Temp [°C]	Specific heat [mJ/(ton·°C)]	Temp [°C]	Elastic modulus [MPa]	Temp [°C]	Coefficient of thermal expansion [1/°C]
30	238	25	9.00E+08	25	73	100	2.06E-05
102	240	100	9.61E+08	54	71	200	2.2E-05
660	209	300	1.02E+09	103	69	300	2.7E-05
656	90	500	1.11E+09	149	67		
701	92	660	1.04E+09	199	65		
795	96	700	1.04E+09	254	63		
1797	116	800	1.06E+09	343	57		

Table 3 Stress–strain behavior

Stress [MPa]	202	261	319	377	435	480
Strain [mm]	0	0.003588	0.012723	0.025961	0.049647	0.099219

Fig. 3 FE meso-scale model for heat transfer analysis

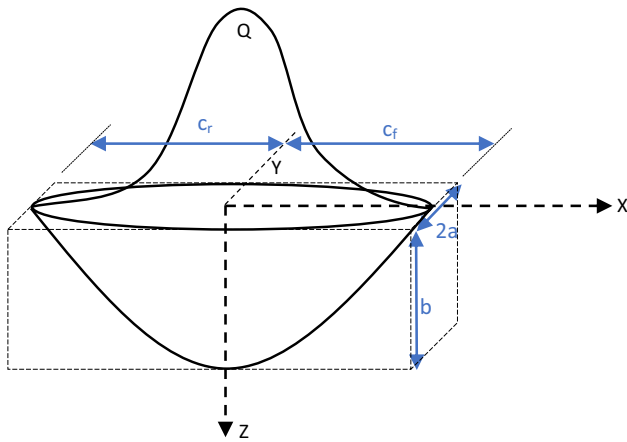
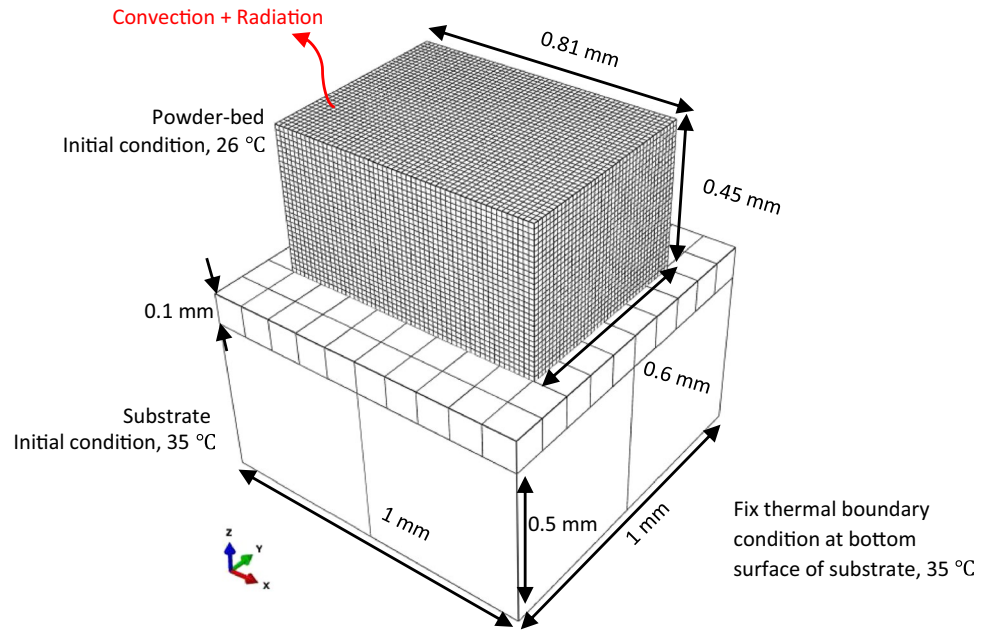


Fig. 4 Goldak function as heat model

$$Q_w = 2\pi k(T - T_o)D + 0.4e\pi\rho C(T - T_o)VD^2 \quad (12)$$

As second step, a full factorial parametric study is carried out with Abaqus using absorption coefficient (from step-1), with the objective to determine the Goldak heat model controlling parameters, i.e., ‘a’, ‘b’, ‘c_f’ and ‘c_r’, which can predict the literature’s melt pool dimensions as shown in Table 4. An initial search space for Goldak parameters was chosen to accommodate the possible maximum and the minimum melt pool (60–560 μm in width and 30–280 μm in depth, whereas length of melt pool was varied 130–480 μm based on c_f+c_r). A total of 288 runs of thermal simulation were carried out and width and depth of melt pool cross sections were captured using python script. In particular, values

Table 4 Melt pool dimensions measured for up-skin layer at 360 W and 1000 mm/s [42]

Melt pool width	2*a	278 μm ± 25
Melt pool depth	b	168 μm ± 25

of the Goldak parameters (independent variables) shown in Table 5 were changed to measure the simulated melt pool width and depth (dependent variables). Image analysis using Matlab (v2022) scripting calculated widths and depths of melt pools for all cases. Peak nodal temperature values were also recorded for each combination.

Laser absorption coefficient and inter layer laser delay time (Infill region) Using best fit Goldak function parameters, absorption coefficient is varied to study its impact on the melt pool overlapping areas and the temperature evolution for the infill region (370 W and 1300 mm/s).

Table 5 Parameters searched space used in parametric study for Goldak heat model

Goldak parameter	Values [mm]
a	0.03, 0.08, 0.13, 0.18, 0.23, 0.28
b	0.03, 0.08, 0.13, 0.18, 0.23, 0.28
c _f	0.03, 0.08, 0.13, 0.18
c _r	0.1, 0.3

Multi-layer temperature evolution (Infill region) Best fit Goldak function parameters are utilized to simulate multi-layer case for the transient temperature evolution for infill region using two different inter layer laser delay times (ILLDT). Since during the computation, temperature at each node is computed after every time increment, to reduce the total time of simulation for a multi-layer case, i.e., multiple layers stacked along build direction or Z-axis, the length of the FE meso-scale model was reduced to 0.405 mm compared to Fig. 3 configuration. This does not affect the heat dissipation behavior due to the melt pool formation since the reduction is along laser travel direction in the XY plane and in this way, the melt pool can be analyzed for subsequent layers without spending too much computational resources. In each deposited layer, a laser (370 W) travels in a straight line from one end to the other at a speed of 1300 mm/s with the absorption coefficient value of 0.4. ILLDT is defined as the time difference between laser off and on instants during the two subsequent layer deposition.

3.2.2 Part-scale simulation

Concentrated heat source Goldak heat source model is not feasible for the part-scale domain due to its high computational cost. Furthermore, finding Goldak function parameters is time-consuming. On the other hand, a concentrated heat source (CHS) [10, 24, 43] or point heat source is simplistic and suitable for the part-scale domain due to its lesser complexity. CHS is considered when element size in FE mesh is larger than source (laser beam) diameter. Far-field temperature predicted by CHS is found to be comparable with temperature measured using thermocouples during PBF process [10], thus, showing the effectiveness of CHS as potential heat source.

Layer-lumping To speed up the simulation process, layer-lumping is considered which merges multiple real powder layers deposited together in a FE mesh to form a consolidated (lumped) layer as illustrated in Fig. 5. It compares a no-lumping case (representing one element per real powder layer thickness (1 E/1 RPL) with the layer-lumped case where one element (edge length) is equivalent to 10 real powder layers (1 E/10 RPL). The main objective is to speed up the overall thermal and structural simulation time so that the final PBF distortions can be compared with the experimentally measured geometric distortions for part-scale.

Part-scale model description (low fidelity) FE-based thermomechanical model is built for the part-scale domain using concentrated heat source (CHS) and layer-lumping approach for the three rectangular plates (Fig. 1), as shown in Fig. 6.

In the FE model, an eight-node linear brick type heat transfer element (DC3D8 in Abaqus) is chosen for uncoupled thermal analysis (TA). Thermal load is applied as a sequential step to the mechanical analysis (MA) where a linear 8-node brick element (C3D8 in Abaqus) is selected for the stress/deformation analysis. Built part is referred to as thin plate.

Model parameters common to thermal and mechanical analysis Two mesh sizes (0.15 mm and 0.3 mm) are varied in the simulation representing 1 E /5 RPL and 1 E/10 RPL cases, respectively. As the average printing time for a real powder layer was 45 s, the time increment was also summed for the five powder layers i.e., $45 \times 5 = 225$ s in 1 E/5 RPL case. Similarly, time increment was chosen to be 450 s for 1 E /10 RPL case. The substrate has been partitioned at top layer with 0.15 mm element from top edge. X-axis and Y-axis of the substrate are sectioned with 3.63 mm long and 1 mm wide elements.

Fig. 5 Layer-lumping illustration (a) no-lumping case 1 E/ RPL (b) layer-lumped 1E/10 RPL

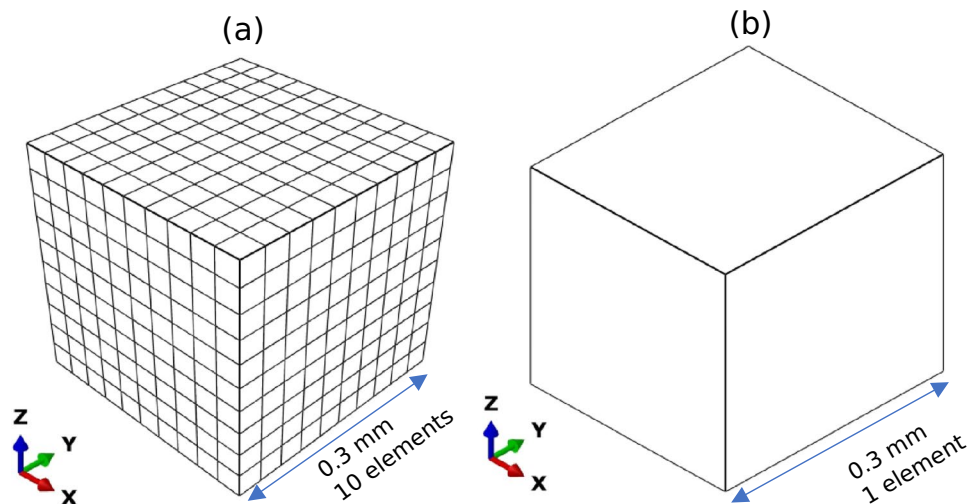
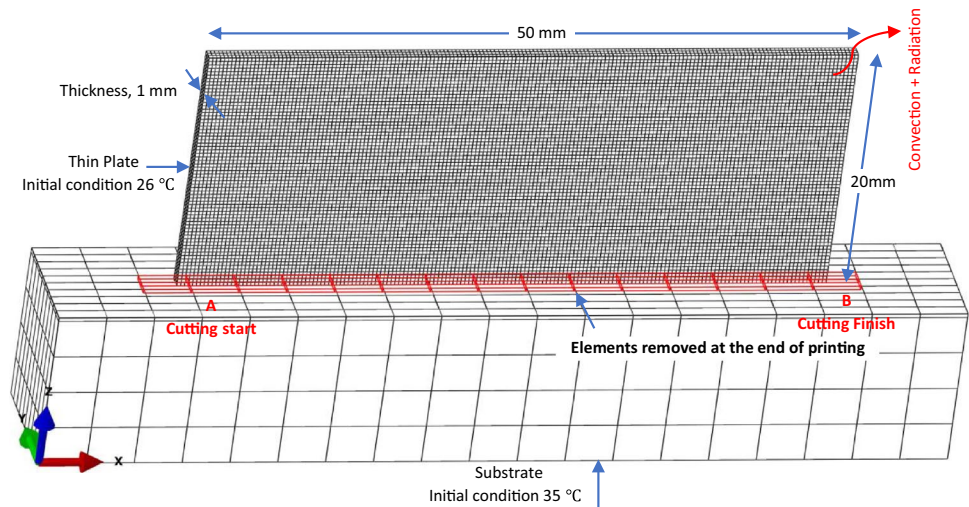


Fig. 6 Part scale model used for printing and elements removal (highlighted in red) from plate-substrate interface as a cutting step. Material used is AlSi10Mg



Abaqus ‘tie’ type constraint is used as connection between the thin plate and the substrate so that heat transfer effect or stress/strain effect due to the printing process and the subsequent removal from the substrate are realistic as in the PBF process. Heat transfer via convection and radiation was considered in both the simulation steps.

Model parameters for TA only An initial predefined field temperature of 26 °C and 35 °C is assigned to the thin plate and to the substrate, following actual printing conditions (Table 1). A fixed temperature boundary condition (35 °C) is applied at the bottom surface of the substrate as during the PBF process the substrate is pre-heated and is kept at the same temperature throughout the simulation.

Model parameters for MA only All translation and rotational movements of the substrate are fixed in all degrees of freedom at the bottom surface of the substrate.

Effect of initial temperature on deformations For the part-scale simulation, preliminary simulations revealed the effect of choosing initial-temperature (T_{initial}) on final built part distortions during the mechanical analysis. T_{initial} values used as input variable in the part-scale simulations are listed in Table 6. This temperature setting is applied as initial predefined field for the thin plates during MA.

Table 6 Input variable summary for the parts-scale: initial temperature and mesh size

Initial temperature (T_{initial}) [°C]	Mesh size (element edge length along X,Y,Z axis)	Mesh notation
100, 125, 150, 175, 200	0.15 mm	1 E /5 RPL
	0.3 mm	1 E /10 RPL

PBF simulation setup in Abaqus In the model, laser processing and activation of mesh elements is manipulated using Abaqus special purpose AM techniques which activate mesh elements and move laser heat source according to their respective eventseries.

An eventseries is a user-defined input to the FE model for describing discrete time instants and space coordinates to start or end an event, e.g., a laser-eventseries will control laser movement (laser speed, power, starting, stopping time) and a roller-eventseries activates mesh elements in FE model, at discrete timepoints and space coordinates. Table 7 presents first few lines in each eventseries type. Laser paths (in X, Y and Z-planes) for contour and infill regions can be precisely defined with such eventseries.

In contrast to 67° rotation in real LPF process, laser rotation for the infill is assumed to be comprised of 0–90° grid by the repetition of horizontal (0°) and vertical (90°) unidirectional [44] laser paths to simplify the model. The total number of layers for 20 mm height was 667 with the exceptional last layer thickness of 20 μm. In roller-eventseries, roller takes up binary values for starting and finishing mesh elements activation. A schematic of 0–90° grid printing strategy is illustrated in Fig. 7.

Irradiation time of odd layers is completed in around 0.52 s for scanning one layer while for even layers, the laser irradiation time is 5 s due to the frequent short delays caused by the ILLDT of 5 ms. Nevertheless, energy delivered to each layer is the same. Laser absorption coefficient of 0.4 is assumed for the part-scale simulation. After all layers are deposited, layers are assumed to be cooled (no further heat addition) for 10 min which is added in both TA and MA simulations.

Table 7 Laser-eventseries (a) Laser paths for first two layers, (b) Roller-eventseries for activating mesh elements

(a) Laser eventseries										(b) Roller eventseries				
Layer-1					Layer-2									
Time(sec)	X	Y	Z	Power(mW)	Time(sec)	X	Y	Z	Power(mW)	Time(sec)	X	Y	Z	On/off
0.33333	0.065	0.065	0.03	320000	45.33333	0.065	0.065	0.06	320000	0.00	0	0.5	0.03	1
0.42239	49.935	0.065	0.03	0	45.42239	49.935	0.065	0.06	0	0.33	50	0.5	0.03	0
0.42239	49.935	0.065	0.03	320000	45.42239	49.935	0.065	0.06	320000	45.00	0	0.5	0.06	1
0.42394	49.935	0.935	0.03	0	45.42394	49.935	0.935	0.06	0	45.33	50	0.5	0.06	0
0.42394	49.935	0.935	0.03	320000	45.42394	49.935	0.935	0.06	320000	90.00	0	0.5	0.09	1
0.51299	0.065	0.935	0.03	0	45.51299	0.065	0.935	0.06	0	90.33	50	0.5	0.09	0
0.51299	0.065	0.935	0.03	320000	45.51299	0.065	0.935	0.06	320000	135.00	0	0.5	0.12	1
0.51455	0.065	0.065	0.03	0	45.51455	0.065	0.065	0.06	0	135.33	50	0.5	0.12	0
0.51455	0.065	0.175	0.03	370000	45.51455	0.175	0.065	0.06	370000	180.00	0	0.5	0.15	1
0.55291	49.935	0.175	0.03	0	45.51522	0.175	0.935	0.06	0	180.33	50	0.5	0.15	0
0.55292	0.065	0.285	0.03	370000	45.51523	0.285	0.065	0.06	370000	225.00	0	0.5	0.18	1
0.59128	49.935	0.285	0.03	0	45.51590	0.285	0.935	0.06	0	225.33	50	0.5	0.18	0
.
.

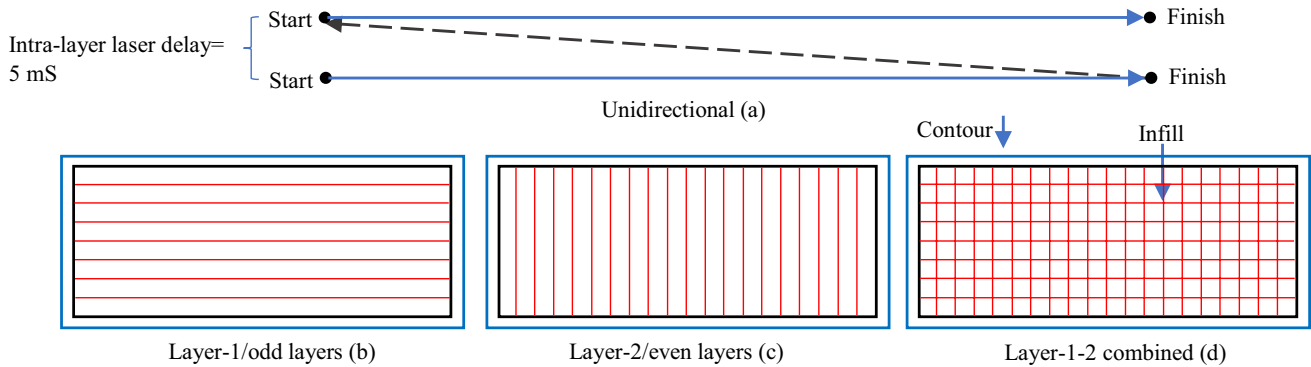


Fig. 7 Laser paths/scanning strategy used in the simulation: (a) unidirectional laser paths (b) layer-1, laser rotation angle 0° (c) layer-2, laser rotation angle 90° (d) layer 1–2 combined, 0–90° grid formed by repetition of all layers. Blue line indicates outer periphery of the part

Plate removal from substrate After the deposition of all the layers, the thin plate is removed/cut from the substrate by deactivating elements using multiple steps and interactions near the thin-plate-substrate interface, replicating the effect of wire cut by electrode discharge machining (EDM) in real scenario. During this cutting phase, elements are removed in direction from point A to B as depicted in Fig. 6. Summary of the PBF simulation stages for the part-scale domain in FE simulation is presented in Fig. 8.

3.3 Length measurement procedure

A visual inspection revealed a slight bending of the edge along XZ plane on both sides. The length of the thin plate is measured at the top, middle and the bottom position as depicted in a Fig. 9. For illustration purpose, exaggerated view of the bent edge is presented which also illustrates the

location of measurements. The top, middle, and the bottom positions are regarding the build direction.

3.3.1 Micrometer

Length of the thin plates were measured along x-axis at three locations (Fig. 9) with Mitutoyo’s digital micrometer having resolution of 0.001 mm. Five measurements were taken at each location.

3.3.2 3D scanning

Printed thin plate (Fig. 1) were optically scanned using the GOM ATOS Core 200 (GOM GmbH, Braunschweig, Germany) 3D coordinate measuring system with a resolution of 0.080 mm. Only one thin plate for each thickness was measured using 3D scanning. The data was analyzed using the

Fig. 8 Summary of stages involved in FE modeling of PBF process

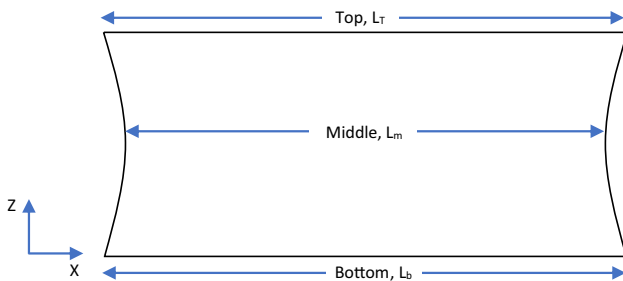
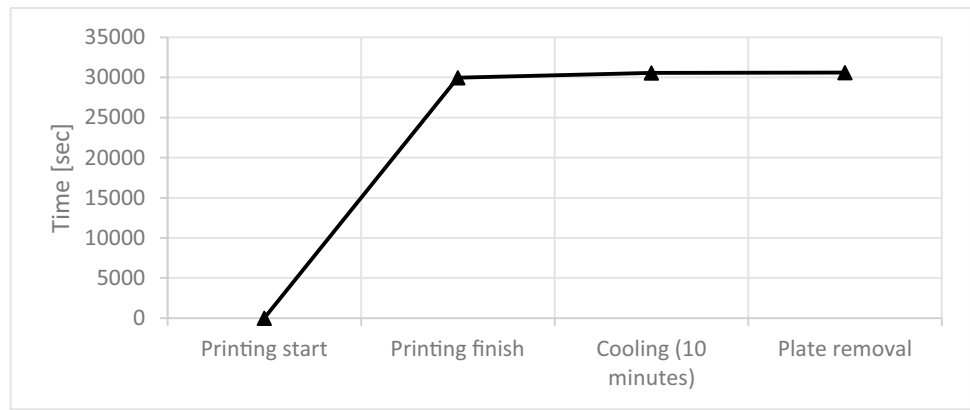


Fig. 9 Length measurement procedure illustration

GOM Inspect 2018 (v2.0.1, GOM GmbH, Braunschweig, Germany) software, which is tested and certified by the National Institute of Standards and Technology (NIST) and the National Metrology Institute of Germany (PTB). Five outer disc measurements were conducted both at the top and at the bottom regions according to Fig. 9. Five outer edge caliper measurements were conducted at the middle region.

3.3.3 Geometric distortion measurement in simulation

In Abaqus, nodal displacement output type UTACT measures the output displacement of a node from the instant it becomes active. As the powder layers are spread in FE model, elements in that layer are activated and start contributing to stiffness of the model.

4 Results and discussion

4.1 Meso-scale model: melt pool and temperature evolution

4.1.1 Melt pool prediction and validation for up-skin region

In most cases, melt pool width and depth are of prime interest since during the melt pool solidification, the length of the

melt pool continuously overlaps with itself and therefore it is difficult to determine without in situ melt pool measurement with any highspeed infrared or CCD cameras [45]. Table 8 enlists the best fit Goldak function parameters for up-skin layer whereas associated prediction error can be found in Table 9.

Rosenthal equation has predicted absorption coefficient of 0.76 which is a pretty large value for aluminum powder whose typical absorption value varies from 0.09 to 0.4 [22, 46–48]. Larger absorption coefficient value could be due to the difficulty in ascertaining some printing parameter values e.g., laser travel speed might not be constant due to acceleration or deceleration at the start and at the end or the temperature dependent material thermal properties could not be very precise thus leading to possible variation in the melt pool size. It is very probable that the actual absorption coefficient is smaller than 0.76 but the true laser traveling speed is smaller than 1000 mm/s and therefore producing large melt pool which otherwise could have been achieved with larger absorption coefficient.

During the simulation, an attempt to increase the width of melt pool result is decreasing the depth of melt pool which is logical since the amount of heat transferred remains

Table 8 Goldak function parameters validated for up-skin region (360 W and 1000 mm/s, absorption coefficient 0.76) for AISi10Mg

Parameters	a	b	c _f	c _r	Temperature (°C)
	0.18	0.23	0.03	0.1	1880

Table 9 Melt pool dimensions: simulation (this research) vs literature results [42]

	Simulation results [mm]	Literature results [mm]	Error
Melt pool width	0.263	0.278	5.4%
Melt pool depth	0.147	0.168	12.5%

constant. Using Goldak parameters in Table 8, simulation predicted melt pool length and width are optimized to reduce the error compared to the literature results for the same printing conditions [42]. As a result of optimization, simulation predicted width of melt pool is 5.4% lower which lies in the acceptable limit while the difference in prediction of depth is larger (error = 12.5%) than the reported melt pool depth [42]. Optimization techniques such as response surface methodology can be further employed to reduce the error; however, these are left out for upcoming research work.

Although the aluminum alloy would melt at around 600 °C but to form large melt pool in up-skin area (as suggested by measurements [42]), it would require high input energy and hence larger melt pool temperature distributions. Such high temperature formation is logical since it would ensure melting of all powder particles in the top layers of up-skin area, reducing the probability of pore formation and ultimately producing better surface finish.

4.1.2 Effect of absorption coefficient (AC) for the infill region

Determining the absorption coefficient (AC) is probably the most crucial parameter when it comes to predicting melt pool dimensions and transient temperature since it controls input heat energy. Simulation results (Fig. 10) revealed expected linear increasing trend of maximum melt pool temperature with increasing AC, which would generate larger melt pool (Table 10).

Results (Table 10, Fig 11, Fig 12) also suggested that optimal value of AC lies between 0.35 and 0.4 since the simulated melt pool overlap would be comparable to printing setup with hatch distance of 0.13 mm and 0.02 mm overlap during real printing process (PBF). However, for simplicity the AC value of 0.4 is chosen in subsequent sections. Predicted melt pool depths suggested remelting will occur

Table 10 Melt pool variation on absorption coefficient

Melt pool dimensions			
Absorption coefficient	Width [mm]	Depth [mm]	Length [mm]
0.3	0.057	0.03	0.069
0.35	0.108	0.068	0.135
0.4	0.143	0.09	0.216

for at least 2 and 3 layers with AC values of 0.35 and 0.4 respectively. Remelting of the previous layer in this context can be beneficial, since it would fuse together the layers homogenously and would increase more strength to the material along built direction, which is typically the weakest due to the layer-by-layer building process of PBF.

4.1.3 Multi-layer case for the infill region

For multi-layer simulation of the meso-model, laser is moved in straight line for 6 layers comprising of 30 μm thickness. The temperature rises and dissipates gradually for such multi-layer case (Fig. 12-b).

An inter-layer laser delay time (ILLDT) of 520 μs might have resulted in some undissipated residual heat after the first track which increases the temperature for the node/layer above when it is exposed to laser. Laser irradiation time for one pass in this case was 312 μs. With these printing parameters, the nodal temperature for node 1 has indicated remelting for three laser passes. Temperature rises when depositing the subsequent layers and thereby number of remelted layers are expected to grow.

To avoid increasing number of remelted layers, ILLDT can be increased, and as the simulation results have suggested (Fig. 13), an even distribution of peak nodal temperatures can be reached by selecting a large enough value

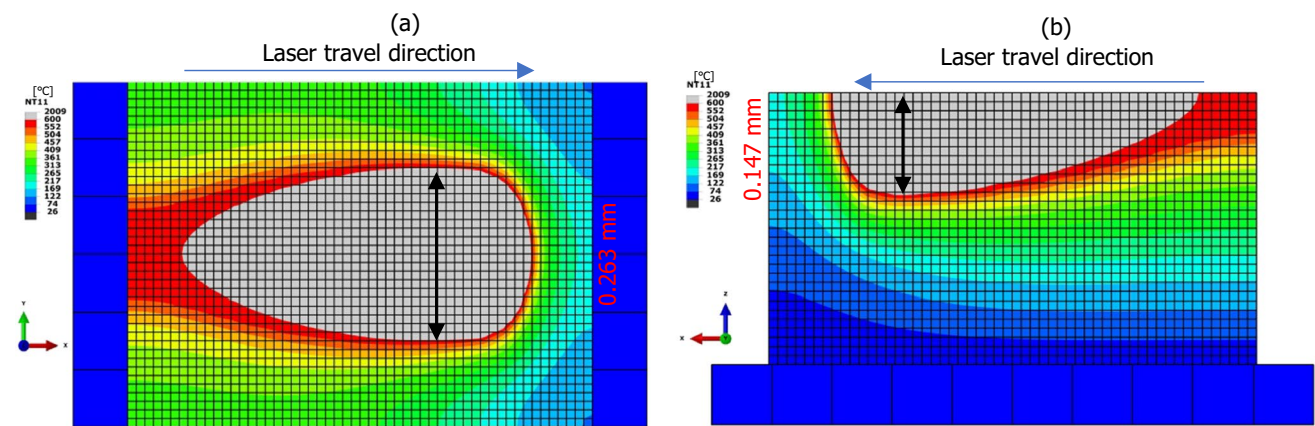


Fig. 10 Melt pool dimension and nodal temperature for up-skin (Power=360 W, speed=1000 mm/s) using the Goldak parameters in Table 8, (a) width, (b) depth (y-section cut) view rotated 180°. Absorption coefficient=0.76, mesh size = 15 μm, material = AISi10Mg

Fig. 11 Rise of maximum temperature with increasing absorption coefficient value

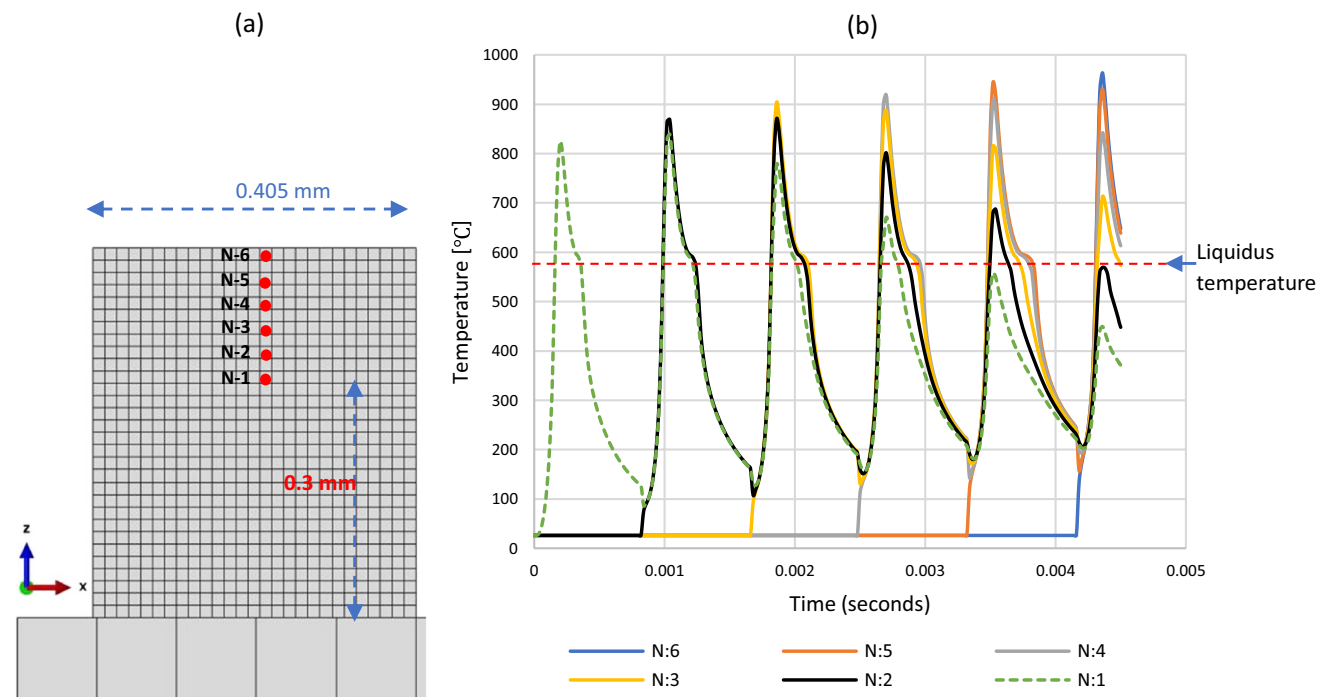
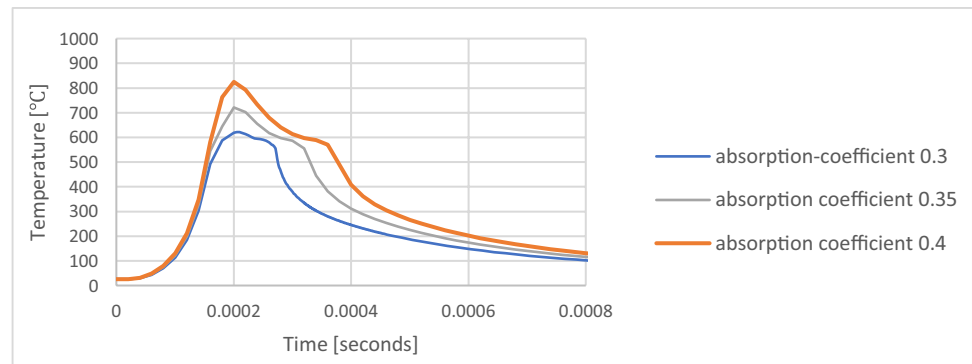


Fig. 12 Multi-layer meso-model for infill region (370 W and 1300 mm/s, AC 0.4), (a) temperature measurement locations, (b) nodal temperature time-history

for ILLDT as was used in the real printing case. Possible reason of such large ILLDT value (45 s) could be scanning of numerous nested components on the substrate and so the laser might have to irradiate all surfaces for one particular height. Nevertheless, an optimal ILLDT should be selected to prevent heat accumulation during the PBF process to avoid remelting of deposited layer.

4.1.4 Meso to part-scale: melt pool comparison using Goldak vs CHS

AC value (0.4) determined through the meso-scale modeling can be used in the part-scale model to keep same energy

input regardless of the heat source model. This approach would combine shorter melt pool and the same AC in the part-scale model which can make sure that the energy balance is satisfied.

Employing concentrated heat source (CHS) reduces required computation resources for thermomechanical analysis. The temperature field distribution and melt pool dimensions as predicted by CHS and the Goldak model are compared in Fig. 14. Simulation results revealed that the temperature elevates to 750 °C using CHS even though the mesh size used is ten times larger than the mesh used for the Goldak heat source model. The simulation results further revealed that temperature reduces to 388 °C with a coarser

Fig. 13 Temperature time evolution, infill region, absorption 0.4 (a) inter-layer laser delay to time (ILLDT) 520 μs (b) ILLDT 45 s

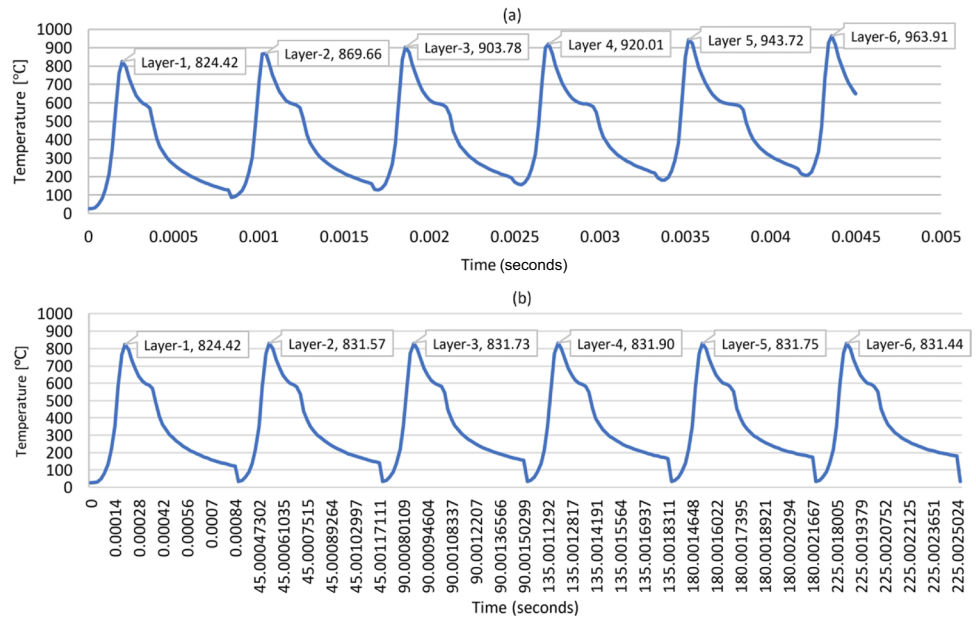
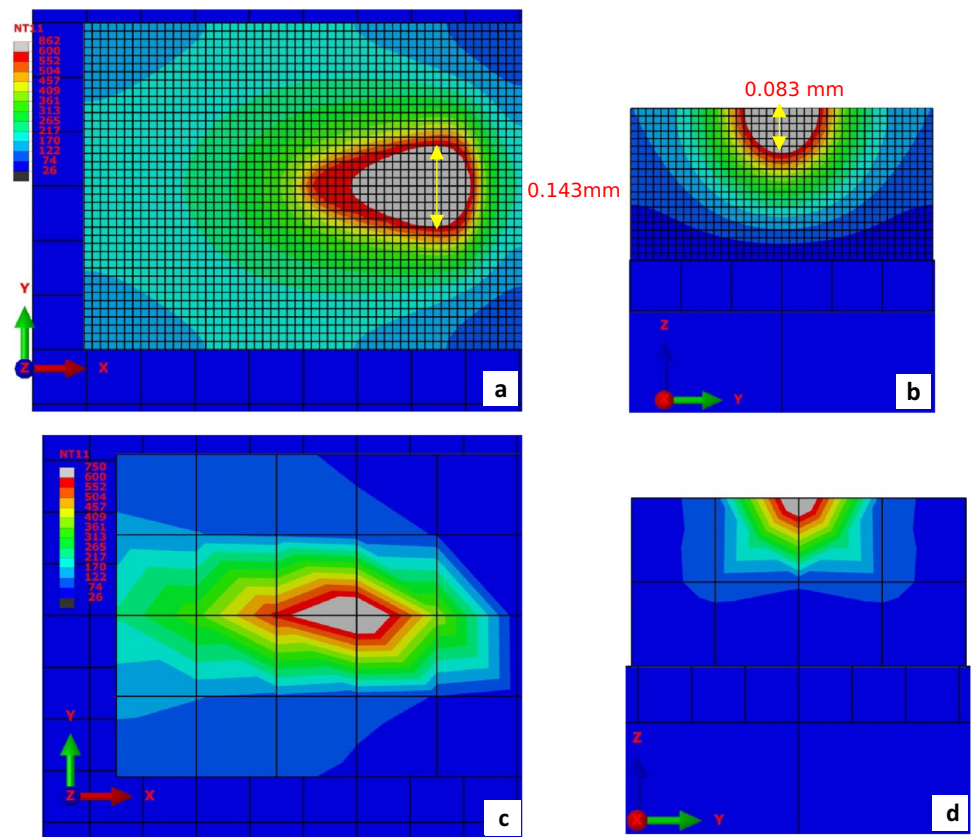


Fig. 14 Melt pool comparison for infill region: Goldak heat source mode (mesh=0.015 mm): melt pool (a) width, (b) depth. Concentrated heat source model (mesh=0.15 mm) (c) width, (d) depth



mesh of 0.3 mm. With large mesh, maximum predicted temperature is expected to decrease significantly since nodes are relatively furthest away and therefore cannot capture high fluctuating transient temperature evolution. Results suggested that CHS is sensitive to the change in mesh size and would affect the subsequent mechanical analysis as well.

4.2 Part-scale: predicting distortions

4.2.1 Experimental distortions

The lengths measured using micrometer and 3d scanning methods of the three plates after removal from the substrate

are presented in Table 11 along with nodal displacement (UTACT) predicted by FE simulations using $T_{initial}$ value of 125 °C. Subsequent sections explain UTACT and its dependency on $T_{initial}$ in more details.

FE simulation results showed no significant nodal movement at the top and at the bottom edges rather the nodes near the center of the plate moved in the opposite direction and that is why only total displacement of two such nodes at the center is shown in the Table 11. For the micrometer and 3D scanning measurements, the length of thin plate measured at top (L_t) and bottom sides (L_b) is larger than at middle (L_m) thereby suggesting slight bending of the edges which is also confirmed by the FE simulation results.

The two measurement methods indicated similar decreasing trend in distortions (L_t-L_m or L_t-L_b); however, the

difference is very small. Decreasing distortions can be attributed to increase in bending resistance due to larger cross sectional with the increase of the thin plate thickness.

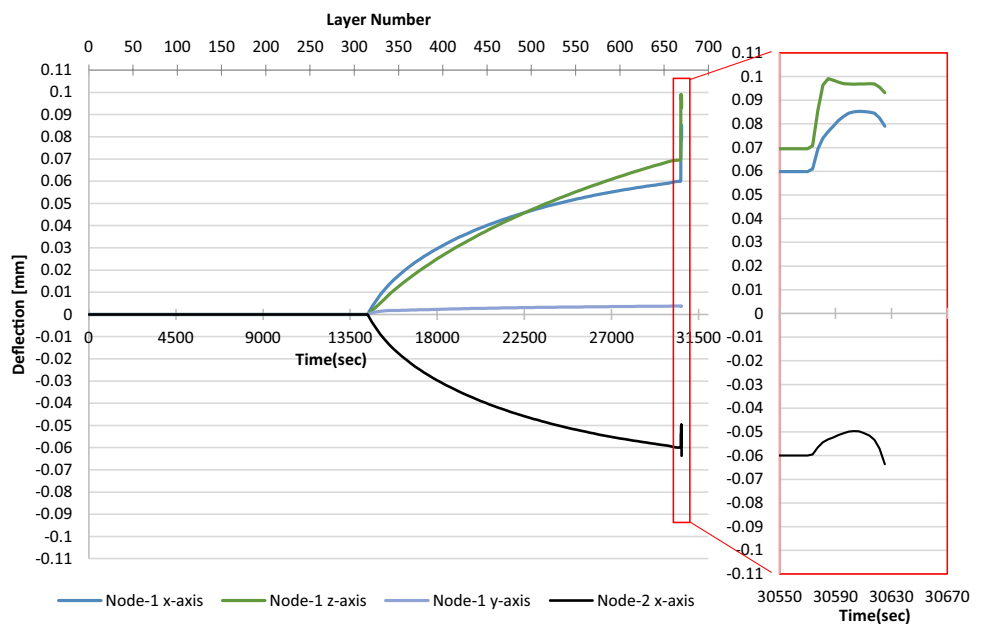
4.2.2 Prediction of AM-induced distortions

The nodal displacements UTACT, extracted after the mechanical simulation at the nodes approximately at midpoint along XZ edges (node-1 and node-2 in Fig. 16) are plotted along X, Y and Z-axis as shown in Fig. 15. During the simulation, a node is activated at the beginning of 320th layer when time was 14,400 s. Before this instant, the node remained inactive in the FE model and did not distort in any direction.

Table 11 Micrometer and 3D scanning results

		Micrometer			3D scanning			FEM simulation
		Average	Standard deviation	Middle-(Top/bottom)	Average	Standard deviation	Middle-(Top/bottom)	$T_{initial} = 125\text{ }^{\circ}\text{C}$ UTACT (mag) left middle node – right middle node
Plate 1 mm	Top Length [mm]	50.510	0.006	0.057	50.595	0.000	0.141	-
	Middle Length [mm]	50.453	0.012	-	50.455	0.012	-	0.112
	Bottom Length [mm]	50.616	0.006	0.163	50.637	0.040	0.183	-
Plate 2 mm	Top Length [mm]	50.548	0.004	0.080	50.546	0.000	0.115	-
	Middle Length [mm]	50.468	0.011	-	50.431	0.004	-	0.116
	Bottom Length [mm]	50.613	0.002	0.145	50.580	0.001	0.149	-
Plate 3 mm	Top Length [mm]	50.561	0.012	0.092	50.552	0.001	0.087	-
	Middle Length [mm]	50.469	0.004	-	50.465	0.007	-	0.117
	Bottom Length [mm]	50.595	0.008	0.126	50.581	0.000	0.116	-

Fig. 15 Nodal displacement along X, Y and Z-axis. (a) Overall PBF process, (b) Plate-removal highlighted. Measurement position: midpoint along XZ-edge



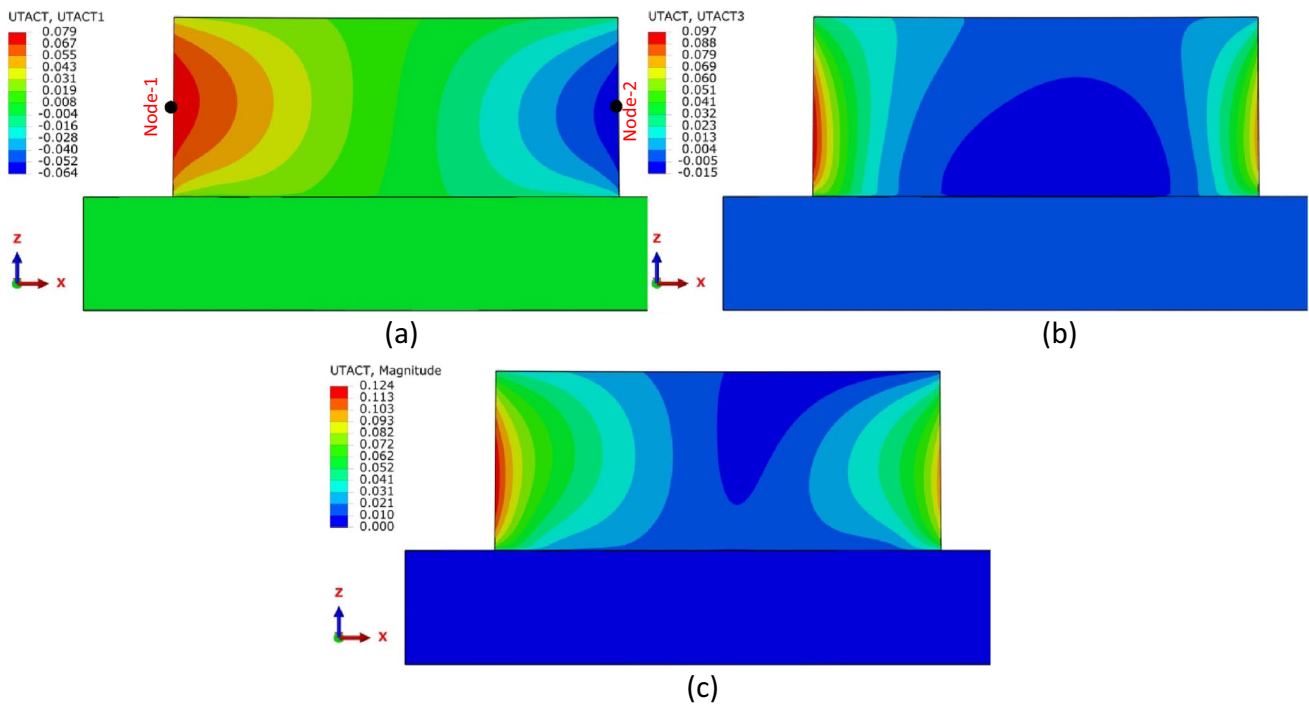


Fig. 16 Nodal displacement (at $T_{initial} = 150^{\circ}\text{C}$) for the 1 mm plate after the substrate removal. Mesh used 0.15 mm or (1E/5PL). (a) UTACT along x-axis, (b) UTACT along z-axis, (c) UTACT magnitude

After the activation, the nodes translated along X- and Z-axis while there was negligible movement along Y-axis (Fig. 15). Considering the 2-dimensional movement of the nodes along XZ-plane, the distortion magnitude is computed and considered as final deflection state of a node. This distortion magnitude is compared with the experimental measurement since a node/point in real PBF process can move freely in 3-dimensional space. Results in Fig. 15 show that during the layer deposition process, node moves or distorts continuously.

The distortion magnitude is computed according to Eq. (13):

$$u_{mag} = \sqrt{(utact_1)^2 + (utact_2)^2 + (utact_3)^2} \tag{13}$$

where utact1, utact2 and utact3 are nodal displacement after activation along X, Y and Z-axis. Final distortion $u_{(mag)}$ is a non-zero scaler quantity and does not indicate the distortion direction.

In Fig. 16, the node-2 has opposite movement after the activation point along X-axis compared to the node-1. The final distortion of two nodes is determined by subtracting their respective displacement magnitudes at the end of substrate removal.

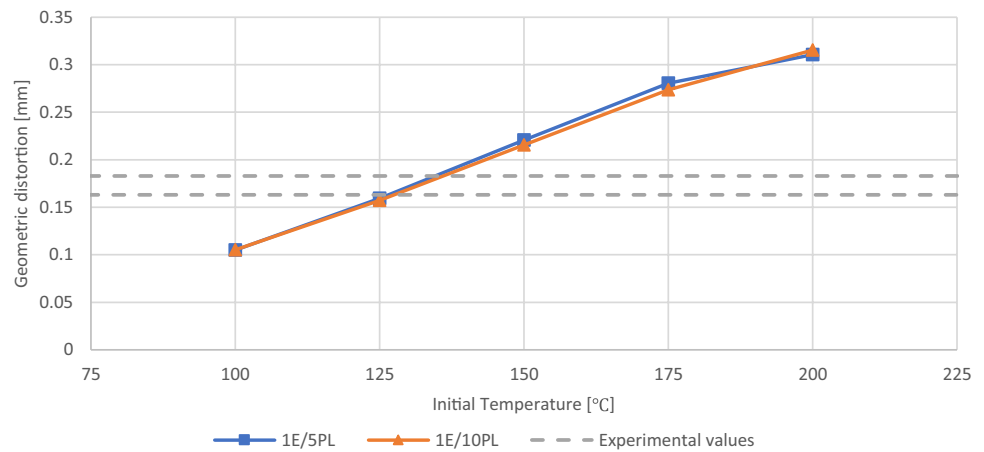
$$u_{total(mag)} = u_{Node-1(mag)} - u_{Node-2(mag)} \tag{14}$$

Nodal displacements are displayed in Fig. 16 after removal from the substrate.

In the subsequent discussion, the final distortion $u_{total(mag)}$ is considered as the measure of predicted geometric distortion. Due to the use of coarse mesh and very large time-increments during thermomechanical simulation, laser irradiation might have been skipped for certain deposited layers and thus only far-field temperature evolution is predicted during the thermal analysis. Consequently, the prediction of the residual stresses and the distortions would be significantly affected during the mechanical analysis. This low magnitude temperature field will not yield appropriate thermal strain that can cause PBF-induced thermal contractions. Thus, the solution requires the addition of a contraction-strain controlling parameter in the mechanical analysis step so that effects of time-skipping (due to time-lumping) and layer-lumping can be counteracted. Equation (8) already relates a simulation parameter ‘initial temperature ($T_{initial}$)’ with the thermal strain which enforces the condition of the zero-strain for newly deposited layer and after layer activation, it adds contracting strains to the previously deposited layers depending on the $T_{initial}$ value.

The nodal distortions $u_{total(mag)}$ are observed to be linearly dependent on $T_{initial}$ as depicted in Fig. 17. The dotted lines in Fig. 17 show the experimental distortion measurements according to Table 11. These values correspond to

Fig. 17 Effect of Initial temperature ($T_{initial}$) on predicted nodal displacement (magnitude) with regard to two mesh sizes for 1 mm thin plate



the two experimental distortion values measured with the 3d scanning and the micrometer, as described in the “Material and methodology” section. Experimental distortions do not depend on initial temperature, which is a simulation parameter only, rather these are displayed in Fig. 17 to visualize and compare with simulation results. The results have shown that the effects of layer and time-lumping on reduced output temperature during thermal analysis can be compensated by tuning the $T_{initial}$ parameter. Results also revealed the effect of mesh size on predicting nodal displacement to be negligible (Fig. 17) and therefore larger meshes, i.e., equivalent to 10 or more real powder layers, can be used for predicting part-scale distortions. This would significantly reduce the computational time for running a thermomechanical model. Simulation time was around 8.5 h with 0.15 mm mesh (1E/5PL case) while it has reduced to much smaller simulation time of 0.2 h using a coarser mesh of 0.3 mm (1E/10PL case). In previous research, although the authors [49] had suggested a methodology to predict $T_{initial}$ value as compensation value for part-scale simulation, but it was not useful for predicting $T_{initial}$ parameter value for aluminum. The challenge of using $T_{initial}$ to compensate layer and time-lumping effects is to determine correct $T_{initial}$ parameter value that can bring about appropriate contraction strains.

4.2.3 Effect of substrate removal and residual stresses

It is observed that geometric distortions were symmetric during the layer deposition process as indicated by Fig. 18-a. After the substrate removal, simulation predicted geometric distortions were asymmetric with higher magnitude along the edges where the cutting initiated. The simulation predicted distortion results match with the experimental distortions, qualitatively.

While with the appropriate $T_{initial}$ value, geometric distortions are within accepted range, the state of residual stresses before and after substrate removal are analyzed to observe the residual stresses which has caused such distortions. The substrate removal after printing process has the most effect on the state of residual stresses as well as on dependent geometric distortions. Figure 19 illustrates the relieving of the built-up residual stresses during and after the layer deposition process.

During the deposition process, the distribution of the residual stresses is symmetric in the thin plate. Large stresses are accumulated at the interface of the thin-plate and the substrate. Upon cutting or when the thin-plate is removed from substrate, significant residual stresses are relieved (Fig. 20-b); nevertheless, high stresses are along outer periphery. Removing these high stress areas might

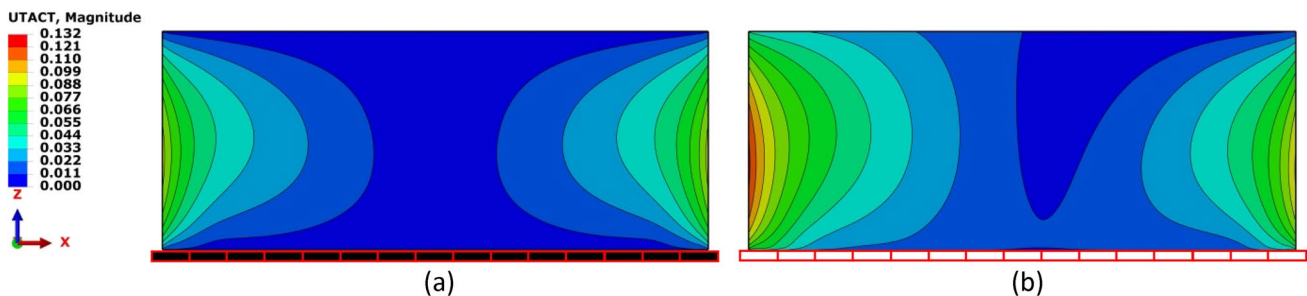


Fig. 18 Plate-1 mm-mesh 0.15 mm (a) end of printing or before substrate removal (b) after substrate removal Black fill = elements are connected, white fill = elements removed

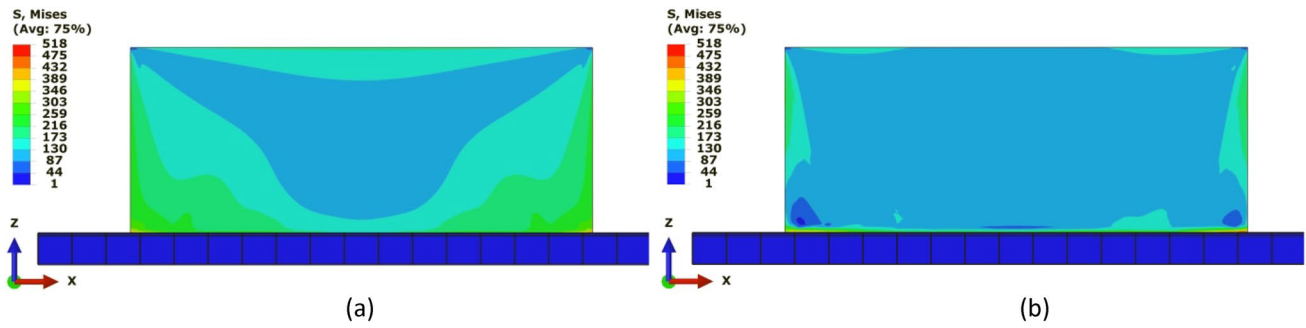


Fig. 19 Mises stress in 1 mm thin plate, mesh 0.15 mm (a) end of printing or before substrate removal (b) after substrate removal

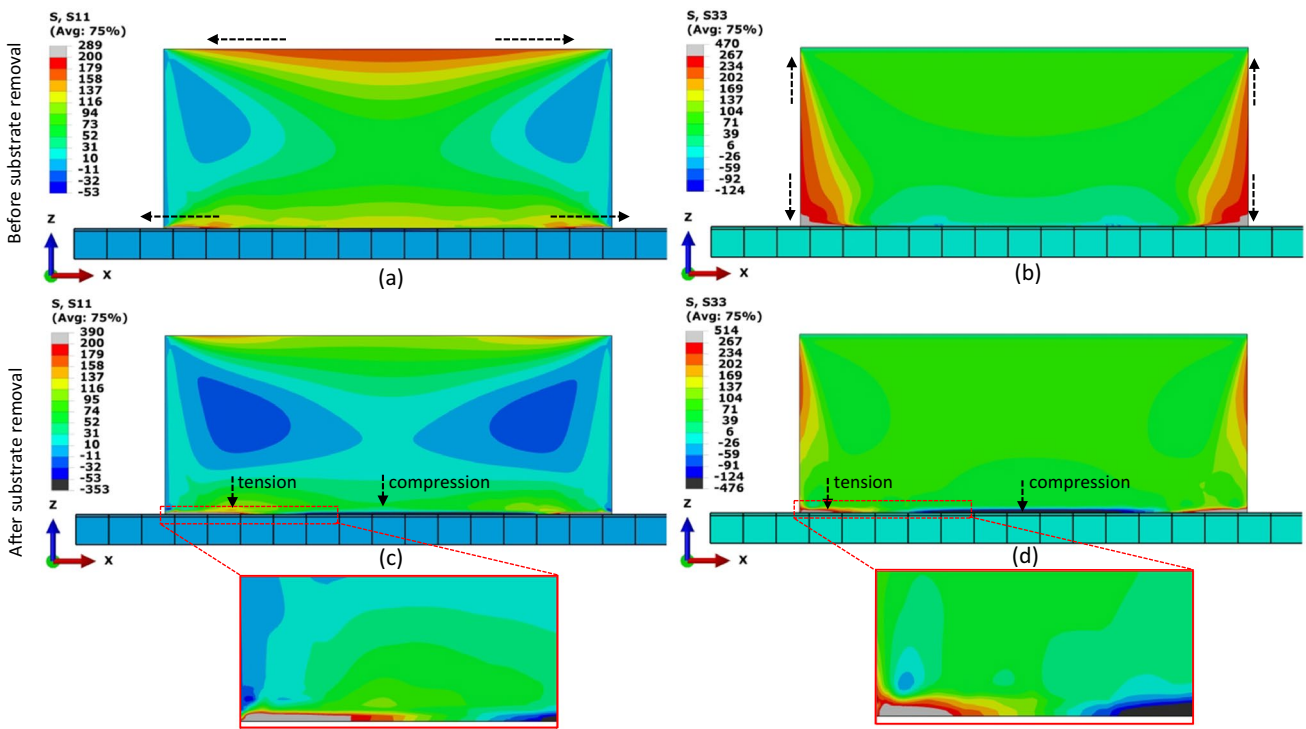


Fig. 20 Residual stresses, before substrate removal: S11 (a) and S33 (b), after substrate removal: S11 (c) and S33 (d)

enhance the built component life, since high residual stresses are prone to fast failures [50].

Longitudinal residual stresses s_{11} and s_{33} are further analyzed before substrate removal (BR) and after substrate removal (AF) cases. Tensile stresses are more evident at the top/bottom edges and at left/right edges of thin-plate in BR case as depicted by Fig. 20-a,b respectively. Here, the last few deposited layers at the top only exhibit tensile stresses along x-axis with almost negligible vertical stress component. The magnitude of the vertical tensile stresses is almost 1.6 times larger than horizontal stresses.

In the AR case, tensile stresses are dominant at the edges and their magnitude is diminished along both directions. Inserts (Fig. 20-c,d) indicate large compressive stresses

originate when the thin-plate is removed from the substrate. Since these stresses are produced after the removal process, they might have little effect on final distortion and probably would be retained. In any case, such high stress zones must be removed via machining or certain heat treatment process.

Based on large tensile stresses along periphery, a distorted shape as predicted in Fig. 21 is suggesting slight bending along both axes. This is in line with the experimental observations as well.

4.2.4 Thickness variation

Simulation results revealed overprediction of geometric distortions for relatively thicker plates at the same $T_{initial}$ value

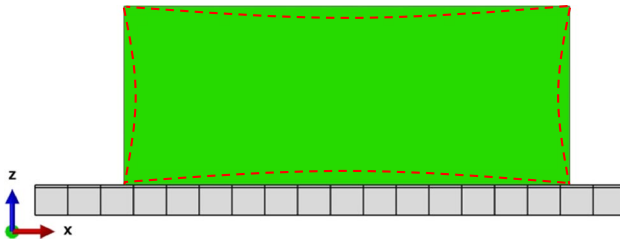


Fig. 21 Illustration of residual stress predicted geometric distortions (red dotted line) after the removal of the thin plate from the substrate

which contradicts the trend observed during experimental length measurement. Red dots in Fig. 22 represent $T_{initial}$ values corresponding to experimental distortion measurement. During the laser-based deposition processes, thermal strain could be thought of having different value for different thicknesses (along y-axis). Since the cross-sectional area increases, the energy input per layer increases as well. To capture such declining distortion trend with increase in plate thickness as indicated by the experimental measurements, $T_{initial}$ value needs to be adjusted by comparing with the experimental distortions. This would require determining geometric distortions experimentally to determine appropriate value of $T_{initial}$ and hence might be cumbersome.

For the simulated distortions of the thin plates (Fig. 22), difference of distortions among the three plates is negligible at 100 °C while the difference grows to maximum of 0.073 mm at 175 °C. It is safe to state that for the three thicknesses, difference of distortions is not significant at a given initial temperature, however the difference is more than threefold for the temperature range of 100–200 °C. Therefore, the impact of choice of initial temperature is much larger and must be carefully determined. For the experimental distortions results, a decreasing trend with increasing thickness has been observed, but due to the conglomeration

of semi-fused particles to the built surface [6], measurements may contain significant uncertainty in reflecting the actual distortions of the edges.

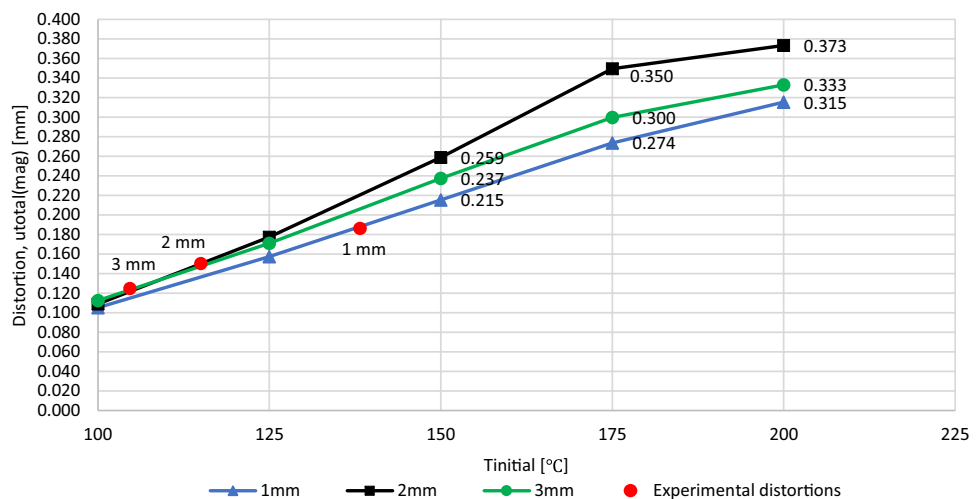
Further, the ability of the model to account for actual plastic distortions can be improved by adopting other plasticity models (e.g., Johnson Cook, Hill48, etc.) and inclusion of plastic strains during the thermal simulations, to accurately predict geometric distortions. It is therefore suggested that at the first stage in the context of current FE simulation approach where large meshes and coarse time steps are adopted, simulation model could be tuned with the physical measurement of the distortions which would determine the $T_{initial}$ parameter and hence would reflect experimental distortions. Considering thickness variation, there is a need to expand the design space for the thickness values and explore the effect of $T_{initial}$ on various thicknesses. A validated FE model can then be used to study and predict the residual stresses effectively, and hence can be employed to analyze the geometric distortions due to the substrate removal via wire EDM processes.

5 Conclusions

A finite-element–based thermomechanical simulation model is used to study the micro and macro properties of the powder bed fusion process (PBF). For micro-scale domain melt pool dimensions, laser absorption and transient temperature evolution are analyzed. Whereas for part-scale domain, geometric distortions are predicted considering parameters such as mesh size, the role of thermal strain, and substrate removal. Conclusions are as follows:

1. Golaik function parameters (i.e., $a = 0.18$, $b = 0.23$, $c_f = 0.03$, $c_r = 0.1$, $f_f = 0.334$, $f_r = 1.667$) can predict melt pool dimension and transient temperature evolu-

Fig. 22 Geometric distortion prediction for different thickness plates



tion. AlSi10Mg absorption coefficient of 0.35–0.4 gives good agreement on predicted melt pool size when compared to experimental hatch spacing. Increasing laser inter-layer delay time reduced temperature rise between deposited layers and prevented excessive remelting.

2. Tensile residual stresses accumulate at the outer periphery of the built part and are relieved during substrate removal. After substrate removal, significant compressive and tensile residual stresses are formed at the built-part substrate interface which can be removed by wire EDM or any heat treatment process.
3. Geometric distortion prediction is less sensitive to mesh size compared to the temperature evolution in the part-scale model.
4. Using large finite element meshes and time steps during thermomechanical simulation yielded far-field temperature which produced significantly small distortions. The solution, however, is to use the additional parameter $T_{initial}$ as a compensation factor in the part-scale model to analyze residual stresses, and geometric distortions appropriately. Thermal strain depends on $T_{initial}$ and can be determined by comparing with experimentally measured distortions.

In this research, the optimal Goldak function parameters for the laser are determined using inverse technique. The overall methodology and the optimal Goldak parameters are the novelty. Optimal parameters can predict the melt pool size and temperature evolution based on absorption coefficient, which can be optimized by comparing with melt pool overlap and hatch distance during real PBF process. As future work, the transient temperature evolution can be further compared with the in situ temperature measurements to verify the determined Goldak parameters. This research emphasized the use of absorption coefficient determined from the meso-scale finite element (FE) simulation which can be used for the part-scale simulation as well. Therefore, a switchover can be made to speed up the simulation while energy balance will be maintained. In this context, a unified approach consisting of two simulation domains (mesoscale and part-scale) can be utilized for the rapid prediction of accurate geometric distortions. The results showed that the mesh sensitivity is a less critical factor affecting accuracy of the results for the mechanical analysis. Crucial factor, however, is to determine the appropriate thermal contraction strain. This work has filled the research gap by analyzing thermo-mechanical simulation parameters selection for commonly used additive manufacturing aluminum alloy, i.e., AlSi10Mg. This has been achieved by measuring geometric distortions and tuning the contraction strain controlling parameter, i.e., initial temperature value, which would eventually control the PBF induced geometric distortions.

The developed FE model with one specific value of initial temperature could not act as a universal value when plate thickness is varied. Therefore, there is a need to establish more efficient method of determining the initial temperature value which can apply required contracting strains, and hence could capture distortion trends. Ideal strategy should be more robust in terms of its application to any change in the geometry of the built component, which is another proposed future research work topic.

Acknowledgements The authors extend their deepest regards to Roy Björkstrand (Aalto University) for providing the additively manufactured plates, printing process parameters and 3D scanning support.

Funding Open Access funding provided by Aalto University. Funding is provided by Aalto University.

Data availability Data can be made available on request.

Declarations

Ethics approval The work was accomplished according to the ICMJE authorship guidelines that comply with ethical standards.

Consent for publication All coauthors are consulted for publication and agree to the consent for publication.

Conflict of interest None declared.

Open Access This article is licensed under a Creative Commons Attribution 4.0 International License, which permits use, sharing, adaptation, distribution and reproduction in any medium or format, as long as you give appropriate credit to the original author(s) and the source, provide a link to the Creative Commons licence, and indicate if changes were made. The images or other third party material in this article are included in the article's Creative Commons licence, unless indicated otherwise in a credit line to the material. If material is not included in the article's Creative Commons licence and your intended use is not permitted by statutory regulation or exceeds the permitted use, you will need to obtain permission directly from the copyright holder. To view a copy of this licence, visit <http://creativecommons.org/licenses/by/4.0/>.

References

1. Akmal JS, Salmi M, Björkstrand R et al (2022) Switchover to industrial additive manufacturing: dynamic decision-making for problematic spare parts. *Int J Oper Prod Manag* 42:358–384. <https://doi.org/10.1108/IJOPM-01-2022-0054>
2. Akmal JS (2022) Switchover to additive manufacturing: dynamic decision-making for accurate, personalized and smart end-use parts. Aalto University
3. Kukko K, Akmal JS, Kangas A et al (2020) Additively manufactured parametric universal clip-system: an open source approach for aiding personal exposure measurement in the breathing zone. *Appl Sci* 10:6671. <https://doi.org/10.3390/app10196671>
4. Wohlers Report 2021. In: Wohlers Assoc. <https://wohlersassociates.com/product/wohlers-report-2021/>. Accessed 5 Feb 2023
5. ISO/ASTM 52900:2015(en), Additive manufacturing — general principles — terminology. <https://www.iso.org/obp/ui/#iso:std:iso-astm:52900:ed-1:v1:en>. Accessed 21 Aug 2022

6. Ullah R, Akmal JS, Laakso SVA, Niemi E (2020) Anisotropy of additively manufactured AlSi10Mg: threads and surface integrity. *Int J Adv Manuf Technol* 107:3645–3662. <https://doi.org/10.1007/s00170-020-05243-8>
7. Ullah R, Akmal JS, Laakso S, Niemi E (2020) Anisotropy of additively manufactured 18Ni-300 maraging steel: threads and surface characteristics. *Procedia CIRP* 93:68–78. <https://doi.org/10.1016/j.procir.2020.04.059>
8. Yang Y, Allen M, London T, Oancea V (2019) Residual strain predictions for a powder bed fusion inconel 625 single cantilever part. *Integrating Mater Manuf Innov* 8:294–304. <https://doi.org/10.1007/s40192-019-00144-5>
9. Ghaoui S, Ledoux Y, Vignat F et al (2020) Analysis of geometrical defects in overhang fabrications in electron beam melting based on thermomechanical simulations and experimental validations. *Addit Manuf* 36:101557. <https://doi.org/10.1016/j.addma.2020.101557>
10. Chen Q, Liang X, Hayduke D et al (2019) An inherent strain based multiscale modeling framework for simulating part-scale residual deformation for direct metal laser sintering. *Addit Manuf* 28:406–418. <https://doi.org/10.1016/j.addma.2019.05.021>
11. Liang X, Chen Q, Cheng L et al (2019) Modified inherent strain method for efficient prediction of residual deformation in direct metal laser sintered components. *Comput Mech* 64:1719–1733. <https://doi.org/10.1007/s00466-019-01748-6>
12. Bruna-Rosso C, Demir AG, Previtali B (2018) Selective laser melting finite element modeling: validation with high-speed imaging and lack of fusion defects prediction. *Mater Des* 156:143–153. <https://doi.org/10.1016/j.matdes.2018.06.037>
13. Schmid S, Krabusch J, Schromm T et al (2021) A new approach for automated measuring of the melt pool geometry in laser-powder bed fusion. *Prog Addit Manuf* 6:269–279. <https://doi.org/10.1007/s40964-021-00173-7>
14. Ransenigo C, Tocci M, Palo F et al (2022) Evolution of melt pool and porosity during laser powder bed fusion of Ti6Al4V alloy: numerical modelling and experimental validation. *Lasers Manuf Mater Process* 9:481–502. <https://doi.org/10.1007/s40516-022-00185-3>
15. Mukherjee T, Zhang W, DebRoy T (2017) An improved prediction of residual stresses and distortion in additive manufacturing. *Comput Mater Sci* 126:360–372. <https://doi.org/10.1016/j.commat.2016.10.003>
16. de Moura NR, de Moraes WA, Vasques MT et al (2021) Role of laser powder bed fusion process parameters in crystallographic texture of additively manufactured Nb–48Ti alloy. *J Mater Res Technol* 14:484–495. <https://doi.org/10.1016/j.jmrt.2021.06.054>
17. Gan Z, Lian Y, Lin SE et al (2019) Benchmark study of thermal behavior, surface topography, and dendritic microstructure in selective laser melting of inconel 625. *Integrating Mater Manuf Innov* 8:178–193. <https://doi.org/10.1007/s40192-019-00130-x>
18. Panwisawas C, Qiu C, Anderson MJ et al (2017) Mesoscale modelling of selective laser melting: thermal fluid dynamics and microstructural evolution. *Comput Mater Sci* 126:479–490. <https://doi.org/10.1016/j.commat.2016.10.011>
19. Dunbar AJ, Denlinger ER, Gouge MF, Michaleris P (2016) Experimental validation of finite element modeling for laser powder bed fusion deformation. *Addit Manuf* 12:108–120. <https://doi.org/10.1016/j.addma.2016.08.003>
20. Calignano F, Manfredi D, Ambrosio EP et al (2013) Influence of process parameters on surface roughness of aluminum parts produced by DMLS. *Int J Adv Manuf Technol* 67:2743–2751. <https://doi.org/10.1007/s00170-012-4688-9>
21. Arisoy YM, Criales LE, Özel T et al (2017) Influence of scan strategy and process parameters on microstructure and its optimization in additively manufactured nickel alloy 625 via laser powder bed fusion. *Int J Adv Manuf Technol* 90:1393–1417. <https://doi.org/10.1007/s00170-016-9429-z>
22. Pei W, Zhengying W, Zhen C et al (2017) Numerical simulation and parametric analysis of selective laser melting process of AlSi10Mg powder. *Appl Phys A* 123:540. <https://doi.org/10.1007/s00339-017-1143-7>
23. Zhang Z, Huang Y, Rani Kasinathan A et al (2019) 3-Dimensional heat transfer modeling for laser powder-bed fusion additive manufacturing with volumetric heat sources based on varied thermal conductivity and absorptivity. *Opt Laser Technol* 109:297–312. <https://doi.org/10.1016/j.optlastec.2018.08.012>
24. Irwin J, Michaleris P (2016) A line heat input model for additive manufacturing. *J Manuf Sci Eng* 138:111004. <https://doi.org/10.1115/1.4033662>
25. Goldak J, Chakravarti A, Bibby M (1984) A new finite element model for welding heat sources. *Metall Trans B* 15:299–305. <https://doi.org/10.1007/BF02667333>
26. Mollamahmutoglu M, Yilmaz O (2021) Volumetric heat source model for laser-based powder bed fusion process in additive manufacturing. *Therm Sci Eng Prog* 25:101021. <https://doi.org/10.1016/j.tsep.2021.101021>
27. Ganeriwala RK, Strantza M, King WE et al (2019) Evaluation of a thermomechanical model for prediction of residual stress during laser powder bed fusion of Ti-6Al-4V. *Addit Manuf* 27:489–502. <https://doi.org/10.1016/j.addma.2019.03.034>
28. Liang X, Hayduke D, To AC (2021) An enhanced layer lumping method for accelerating simulation of metal components produced by laser powder bed fusion. *Addit Manuf* 39:101881. <https://doi.org/10.1016/j.addma.2021.101881>
29. Mohammadtaheri H, Sedaghati R, Molavi-Zarandi M (2022) Inherent strain approach to estimate residual stress and deformation in the laser powder bed fusion process for metal additive manufacturing—a state-of-the-art review. *Int J Adv Manuf Technol* 122:2187–2202. <https://doi.org/10.1007/s00170-022-10052-2>
30. Liu S, Zhu H, Peng G et al (2018) Microstructure prediction of selective laser melting AlSi10Mg using finite element analysis. *Mater Des* 142:319–328. <https://doi.org/10.1016/j.matdes.2018.01.022>
31. MehrabanTeymouri R, Panwisawas C, Ravani B (2022) Multi-scale modeling for multi-track multi-layer laser powder bed fusion additive manufacturing: a material dependent melt pools, microvoid defects and mechanics study
32. Jia Y, Saadlaoui Y, Roux J-C, Bergheau J-M (2022) Steady-state thermal model based on new dedicated boundary conditions – application in the simulation of laser powder bed fusion process. *Appl Math Model* 112:749–766. <https://doi.org/10.1016/j.apm.2022.08.013>
33. Cheng J, Huo Y, Fernandez Zelaia P et al (2022) A Gaussian process-based extended Goldak heat source model for finite element simulation of laser powder bed fusion additive manufacturing process. Available at: <https://ssrn.com/abstract=4207472>; <https://doi.org/10.2139/ssrn.4207472>
34. Magerramova L, Isakov V, Shcherbinina L et al (2022) Design, simulation and optimization of an additive laser-based manufacturing process for gearbox housing with reduced weight made from AlSi10Mg alloy. *Metals* 12:67. <https://doi.org/10.3390/met12010067>
35. Aktürk M, Boy M, Gupta MK et al (2021) Numerical and experimental investigations of built orientation dependent Johnson-Cook model for selective laser melting manufactured AlSi10Mg. *J Mater Res Technol* 15:6244–6259. <https://doi.org/10.1016/j.jmrt.2021.11.062>
36. An N, Yang G, Yang K et al (2021) Implementation of Abaqus user subroutines and plugin for thermal analysis of powder-bed electron-beam-melting additive manufacturing process. *Mater Today Commun* 27:102307. <https://doi.org/10.1016/j.mtcomm.2021.102307>

37. Additive manufacturing - SIMULIA User Assistance (2022) https://help.3ds.com/2022/english/DSSIMULIA_Established/SIMACAEANLRefMap/simaanl-m-AdditiveManufacturingProcessSimulation-sb.htm?contextscope=all. Accessed 7 Mar 2022
38. Hu H, Ding X, Wang L (2016) Numerical analysis of heat transfer during multi-layer selective laser melting of AlSi10Mg. *Optik* 127:8883–8891. <https://doi.org/10.1016/j.ijleo.2016.06.115>
39. 3d Print Aluminum | Metal 3D printing. <https://www.eos.info/en/additive-manufacturing/3d-printing-metal/dmls-metal-materials/aluminium-al>. Accessed 7 Mar 2022
40. Van Cauwenbergh P, Anthony B, Lore T et al (2018) Heat treatment optimization via thermo-physical characterization of AlSi7Mg and AlSi10Mg manufactured by laser powder bed fusion (LPBF). Proceedings of the EuroPM 2018 Congress, Bilbao, Spain
41. Romero J, Toledo G, Saha B (2016) Deformation and residual stress based multi-objective genetic algorithm for welding sequence optimization. *Research in Computing Science* 132:155–179. <https://doi.org/10.13053/rcs-132-1-12>
42. Tang M (2017) Inclusions, porosity, and fatigue of AlSi10Mg parts produced by selective laser melting. Ph.D Thesis, University Pittsburg, Pittsburgh, PA, USA
43. Thermomechanical analysis of powder bed-type additive manufacturing processes using the trajectory-based method - SIMULIA user assistance 2022. https://help.3ds.com/2022/english/dssimulia_established/SIMACAEANLRefMap/simaanl-c-amspecialpurpose-powderbed.htm?contextscope=all#simaanl-c-amspecialpurpose-powderbed-concentratedheat. Accessed 7 Mar 2022
44. Marattukalam JJ, Karlsson D, Pacheco V et al (2020) The effect of laser scanning strategies on texture, mechanical properties, and site-specific grain orientation in selective laser melted 316L SS. *Mater Des* 193:108852. <https://doi.org/10.1016/j.matdes.2020.108852>
45. Liu Y, Wang L, Brandt M (2021) An accurate and real-time melt pool dimension measurement method for laser direct metal deposition. *Int J Adv Manuf Technol* 114:2421–2432. <https://doi.org/10.1007/s00170-021-06911-z>
46. Ansari P, Salamci MU (2022) On the selective laser melting based additive manufacturing of AlSi10Mg: the process parameter investigation through multiphysics simulation and experimental validation. *J Alloys Compd* 890:161873. <https://doi.org/10.1016/j.jallcom.2021.161873>
47. Liu C, Li C, Zhang Z et al (2020) Modeling of thermal behavior and microstructure evolution during laser cladding of AlSi10Mg alloys. *Opt Laser Technol* 123:105926. <https://doi.org/10.1016/j.optlastec.2019.105926>
48. Gu D, Yang Y, Xi L et al (2019) Laser absorption behavior of randomly packed powder-bed during selective laser melting of SiC and TiB₂ reinforced Al matrix composites. *Opt Laser Technol* 119:105600. <https://doi.org/10.1016/j.optlastec.2019.105600>
49. Ullah R, Lian JH, Wu JJ, Niemi E (2022) Effect of finite element mesh size and time-increment on predicting part-scale temperature for powder bed fusion process. *Key Eng Mater* 926:341–348. <https://doi.org/10.4028/p-16auf3>
50. Withers PJ (2007) Residual stress and its role in failure. *Rep Prog Phys* 70:2211–2264. <https://doi.org/10.1088/0034-4885/70/12/R04>

Publisher's note Springer Nature remains neutral with regard to jurisdictional claims in published maps and institutional affiliations.